Energy materials

Growth of Bi$_2$Se$_3$/graphene heterostructures with the room temperature high carrier mobility

I. V. Antonova[1,2,*] , N. A. Nebogatikova[1,3], N. P. Stepina[1], V. A. Volodin[1,2], V. V. Kirienko[1], M. G. Rybin[3,4], E. D. Obrazstova[3,4], V. A. Golyashov[1], K. A. Kokh[2,5,6], and O. E. Tereshchenko[1,2]

[1] Rzhanov Institute of Semiconductor Physics SB RAS, Lavrentiev av. 13, Novosibirsk, Russia 630090

[2] Novosibirsk State University, Pirogova str., 1, Novosibirsk, Russia 630090

[3] Prokhorov General Physics Institute, RAS, Vavilov str. 38, Moscow, Russia 119991

[4] Moscow Institute of Physics and Technology (State University), Kerchenskaya str. 1a, Moscow, Russia 117303

[5] Kemerovo State University, Krasnaya str., 6, Kemerovo, Russia 650000

[6] Sobolev Institute of Geology and Mineralogy, Koptyug av. 3, Novosibirsk, Russia 630090

ABSTRACT

Heterostructures of Bi$_2$Se$_3$ topological insulators were epitaxially grown on graphene by means of the physical vapor deposition at 500 °C. Micrometer-sized flakes with thickness 1 QL (quintuple layer $\sim$ 1 nm) and films of millimeter-scale with thicknesses 2–6 QL had been grown on CVD graphene. The minimum thickness of large-scaled continuous Bi$_2$Se$_3$ films was found to be $\sim$ 8 QL for the regime used. The heterostructures with a Bi$_2$Se$_3$ film thickness of > 10 QL had resistivity as low as 200–500 Ω/sq and a high room temperature carrier mobility $\sim$ 1000–3400 cm^2/Vs in the Bi$_2$Se$_3$/graphene interface channel. Moreover, the coexistence of a p-type graphene-related conductive channel, simultaneously with the n-type conductive surface channel of Bi$_2$Se$_3$, was observed. The improvement of the bottom Bi$_2$Se$_3$/graphene interface with the increase in the growth time clearly manifested itself in the increase of conductivity and carrier mobility in the grown layer. The grown Bi$_2$Se$_3$/G structures have lower resistivities and more than one order of magnitude higher carrier mobilities in comparison with the van der Waals Bi$_2$Se$_3$/graphene heterostructures created employing exfoliation of thin Bi$_2$Se$_3$ layers. The grown heterostructures demonstrated the properties that are perspective for new functional devices, for a variety of signal processing and logic applications.

Introduction

Two-dimensional (2D) materials, normally referred to as single-layer materials, have become a central topic of research interest over the past 20 years [1, 2]. Understanding the physics of these novel layered materials has provided a great platform for the potential opportunities in many fields ranging from electronics, optoelectronics to energy, sensing, biological and medical applications, including the development of flexible electronics [3, 4]. The weak van der Waals interaction (as compared to the strong covalent bond interaction inside covalently bonded material structures) made it possible to construct promising building blocks for future electronics and optoelectronics by stacking 2D materials with multidimensional materials to form van der Waals heterostructures. The development of technologies of synthesis or layer-by-layer growth of vertical heterostructures from different 2D materials is the most important approach for future progress in these novel electronics [5, 6]. Graphene is now widely used as a substrate for the growth of 2D materials or quantum dots. Graphene often increases growth rates, improves structure of grown materials, or can serve as an excellent sub-nm spacer and create a uniform nanogap between different layers in heterostructures [7–10].

The discovery of the three-dimensional topological insulator (TI) as a quantum state of matter has expanded the family of Dirac materials with applications in electronics, spintronics, and quantum computing [11]. TI materials are distinguished by their strong intrinsic spin–orbit coupling, which leads to the formation of a bulk bandgap and 2D surface states that host massless Dirac Fermions with spin-momentum locking [12]. Topological insulators are predicted to present unique surface transport phenomena, but their experimental studies have been hindered by metallic bulk conduction that overwhelms the surface transport [13–15]

Nowadays, topological insulator/graphene (TI/G) heterostructures are considered as a way to combine the spin-dependent TI properties with high electron mobility. Despite a sound understanding of the two individual materials (TI and graphene), the electron transport of a combined vertical heterojunction is still poorly studied. For instance, enhancing the spin–orbit interaction in graphene via proximity effects with topological insulators in TI/G heterostructures could create a novel 2D system that combines nontrivial spin textures with high electron mobility, as revealed in the theoretical study of Song [6]. These calculations predict the emergence of giant spin lifetime anisotropy in graphene layer, which should be a measurable hallmark of spin transport in TI/G heterostructures and suggest novel types of spin devices. The anomalous magnetotransport effects, gate-tunable tunneling resistance, and the possible existence of a quantum spin Hall phase are reported in TI/G heterostructures with Bi_2Se_3, Bi_2Te_3, and other materials [12, 16–18]. In addition, the fabrication of broadband photodetectors based on TI/G heterostructures [19] and the injection of a spin-polarized current from ultrathin Bi_2Te_2Se nanoplatelets into graphene [20] has been realized. It was demonstrated that the graphene provides a high-quality interface with thick (400 nm) Bi_2Se_3 films and carrier mobility on topological surface states as high as ~ 5000 cm^2/Vs at low temperature (2 K) without degradation [21]. Moreover, the nonlinear field dependence of Hall resistivity at low magnetic fields [22] suggests the presence of additional conducting channels with higher carrier mobility [23–25].

In addition to spintronics, thin TI/G films have great potential for use in vertical 2D material heterostructures as a channel with high conductivity instead of just graphene, if its resistance will be reduced in comparison to the case of using graphene. The typical graphene sheet resistance is 1–2 kOhm/sq [26–28]. Moreover, low resistance films could be applied, for instance, as transparent electrodes for the IR range where Bi_2Se_3 has very low absorption [29].

In this study, we present Bi_2Se_3-based heterostructures in TI/graphene/SiO_2/Si configuration, using the CVD grown graphene, the deposited Bi_2Se_3 films, and Si substrate as the gate to control the Fermi level position. For heterostructures with TI film thickness 20–50 nm (the resistivity as low as 200–500 Ω/sq), the coexistence of *n*- and *p*-type channels and the high room temperature carrier mobility up to ~ 3400 cm^2/Vs for n-type channel of Bi_2Se_3 films were found. The grown Bi_2Se_3/G heterostructures have a higher quality and perspective for application properties.

Experimental

Sample preparation

Graphene was synthesized using the method of chemical deposition in the gas phase, implemented in a cold wall installation and resistive heating of copper foil using a current $\sim$ 70 A. Methane introduction into the chamber at a concentration of 3% at a temperature of 850 °C for 5 min leads to a growth of graphene. The transfer of graphene from copper foil to a 300 nm SiO_2/Si substrate is carried out using standard technology using PMMA as a supporting polymer. Treatment in acetone followed by rinsing in isopropyl alcohol was used for PMMA removal. The resulted graphene has the p-type conductivity with resistivity $\sim$ 0.9–1.3 kOhm/sq and carrier mobility of 1000–2000 cm^2/Vs.

The growth of Bi_2Se_3 films was performed using the physical vapor deposition at the source temperature of 500 °C for time 7–40 h. These heterostructures will be hereinafter referred to as BS/G structures.

For second type heterostructures, the thin Bi_2Se_3 flakes were obtained using electrochemical exfoliation. Bi_2Se_3 was used as a cathode; an electrolyte was ammonium sulfate with a concentration of 1%. Electrochemical exfoliation leads to the creation of Bi_2Se_3 flakes with a thickness of 4 and 8 nm and lateral size up to $\sim$ 100 mm. Then, these flakes were transferred onto G/SiO_2/Si substrates. Below, these structures will be denoted as vdW-BS/G.

Experimental equipment

The Raman spectra were recorded on a Horiba Jobin Yvon LabRAM HR800 spectrometer with a 1024-pixel LN/CCD detector and an Nd:Gd 532 nm laser under ambient conditions with power $\sim$ 1 mW. The spectral resolution was approximately 3.0 cm^{-1} at a frequency shift of 1300 cm^{-1}. The integration time was 6 min. Raman spectra with different polarization were recorded on a triple T64000 Horiba Jobin Yvon spectrometer at room temperature, with the excitation wavelength being 514.5 nm (2.41 eV argon ion laser). To avoid the heating of samples with laser radiation, the laser beam was defocused up to a spot diameter of 30 mm. A Solver PRO NT-MDT scanning microscope was employed for taking AFM images from the surface of examined films and substrates

and for evaluating the sample thicknesses. The measurements were carried out in contact and semi-contact modes. The rounding radius of the used probe never exceeded 10 nm; normally, it was equal to $\sim$ 2–3 nm. Apart from the study of the surface relief, measurements in lateral-force (friction-force) mode were carried out for visualization of regions differing in their chemical compositions. The current–voltage characteristics were measured with a Keithley picoamperemeter (model 6485) on film samples provided with contacts prepared from silver alloy or indium soldering. X-ray diffraction analysis data were collected on an ARL'Xtra diffractometer in the Bragg–Brentano geometry (2θ = 10–60°, CuK_{α} — radiation, U = 30–40 kV, I = 25 mA). SEM images were obtained using a JEOL JSM-7800F scanning electron microscope in which the energy of primary electrons was equal to 2 keV.

Experimental results

Structural properties of the Bi_2Se_3/graphene/SiO_2/Si heterostructures

Figure 1 demonstrates the sketch of the growth reactor and the optical images of Bi_2Se_3 film grown on 5 × 10 mm graphene transferred onto the SiO_2/Si sample. In the left part of Fig. 1b1 (the region near the source), one can see Bi_2Se_3 nanoparticles grown on SiO_2/Si substrate. AFM studies of Bi_2Se_3 /SiO_2/Si show that this part consists of Bi_2Se_3 particles with the size of $\sim$ 0.5–1 μm, the thickness $\sim$ 30–35 nm, and the surface relief up to 100 nm. The relatively high resistivity of 2–3 kOhm/sq was found for Bi_2Se_3 clusters in the part grown on SiO_2/Si. At the right of the SiO_2/Si sample (Fig. 1b3) without graphene, the Bi_2Se_3 was not grown at all. Directly on graphene, the continuous film was grown with a thickness of 50–20 nm (from left to right). Generally, for samples shifted from the source on more than 1 cm, Bi_2Se_3 films were grown only on graphene with high selectivity.

Variation in a growth time shows that islands of Bi_2Se_3 monolayer flakes are observed first (Fig. 2). The relatively large Bi_2Se_3 domain size (few micrometers) from one fold to another fold is seen in Fig. 2b, c. The height of folds is 2–6 nm. The films of millimeter-scale with thickness 2–6 nm were grown with an increase in the growth time (Fig. 3a).
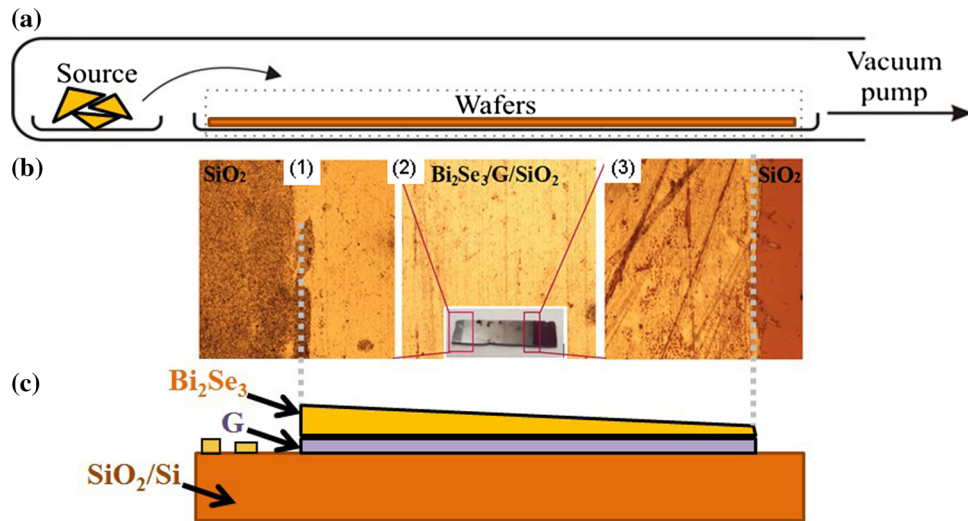
Figure 1 **a** Scheme of the growth reactor. The source temperature was equal to 500 °C, and the temperature in the sample area decreases ∼ 450 °C. **b** An image of the Bi2Se3 film grown at 500 °C (22 h) on the SiO2 substrate with transferred CVD graphene (the length of the graphene film was 10 mm) made in the optical microscope, inset in **b** presents an optical image of the sample with Bi2Se3/graphene film. (1) Optical microscopy image of the beginning part of the sample (near the precursor source): the dark part corresponds to Bi2Se3 film grown on the SiO2 substrate, and the light part corresponds to Bi2Se3 film grown on the G/SiO2 substrate; (2) the middle part of the sample; (3) the end of the grown Bi2Se3 film. According to AFM data, the Bi2Se3/G film thickness is varied from 50 to 20 nm as a function of the distance from the source. The sizes of the (1,2,3) images are 0.25 mm × 0.25 mm. **c** Schematic image of the sample cross section.
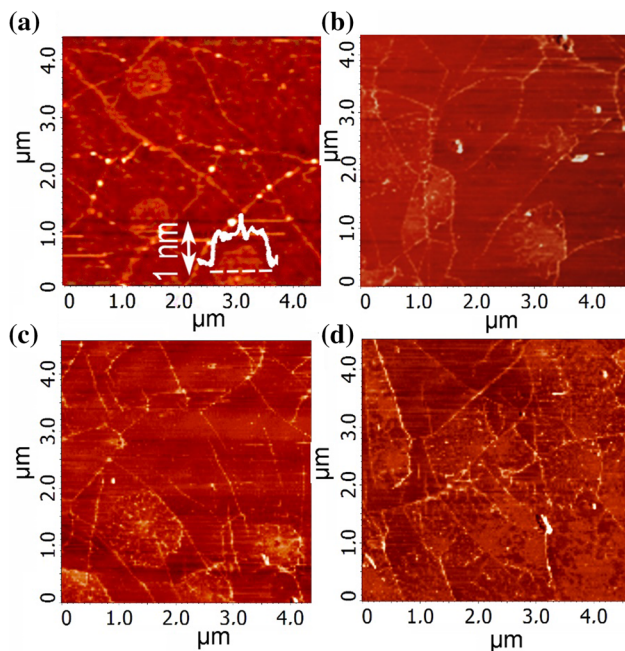

Figure 2 The initial stage of Bi_2Se_3 film growth at 500 °C on CVD grown graphene. **a**–**d** The surface images of samples grown for 7–10 h measured in **a** height and **b**–**d** lateral force modes. Bi_2Se_3 light islands are placed between the folds visible on graphene. Profiles cross the Bi_2Se_3 islands in **a** demonstrate the thickness of ∼ 1 nm. **b**, **c** Bi_2Se_3 islands with size from one fold to another fold.

Nanoparticles with higher thickness are seen on film in this case. The continuous film has a thickness of ∼ 8 nm; this thickness was directly measured near the graphene edge (Fig. 3b). The further increase in growth time leads to the synthesis of the film with a thickness gradient of 50–20 nm on 10 mm length. Therefore, the grown film has a uniform thickness at the millimeter scale. AFM images of Bi_2Se_3 film with thickness 50 nm grown on the $G/SiO_2/Si$ substrate are given in Fig. 4a. It is seen that this film has a surface relief of less than 10 nm.

The edge of the grown Bi_2Se_3 film exactly coincides with the edge of the graphene. The maximum thickness of 200 nm was found for a growth time of 40 h. AFM image of this Bi_2Se_3 film and image of the surface measured in the regime of lateral forces (Fig. 4c) demonstrate the surface with ∼ 15 nm pyramid-like relief consisted of 1-nm Bi_2Se_3 quintuple layers. In Bi_2Se_3, five covalently bonded atomic sheets (e.g., Se–Bi–Se–Bi–Se) compose one quintuple layer (QL, ∼ 1 nm) [30, 31]. The grown set of samples is marked as BS/G-1 ÷ BS/G-7 depending on the thickness (see Table 1). The SEM images of the two films are given in Fig. 4d. The SEM and AFM images demonstrate that grown film has a polycrystalline structure with a relatively large domain size. The pyramids in

Figure 3 The intermediate stage of Bi_2Se_3 film growth at 500 °C on graphene: **a** a continuous film with thickness $\sim$ 8 nm and **b** a film with thickness $\sim$ 10 nm.
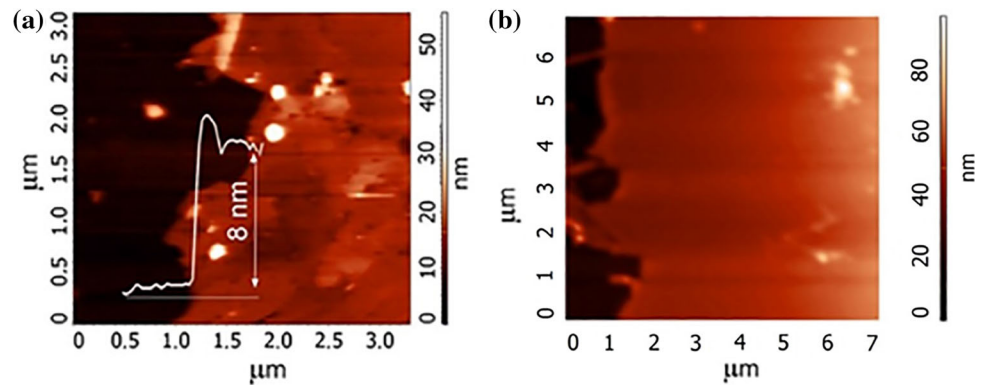

Figure 4 AFM images of Bi_2Se_3 film grown at 500 °C (22 and 40 h) on the graphene transferred on SiO_2/Si sample: **a** for film thickness 60 nm and **b** 200 nm. The profiles along the surface (**a**) and the cross edge of Bi_2Se_3 film (**b**) are presented in inserts. **c** Lateral force image of the 200 nm film with up to 15 nm surface relief in the form of pyramids from Bi_2Se_3 monolayers. Insert demonstrates the surface relief. **d** SEM images of the Bi_2Se_3 film grown at 500 °C on the CVD grown graphene transferred on SiO_2/Si sample with the film thickness of 20 nm.
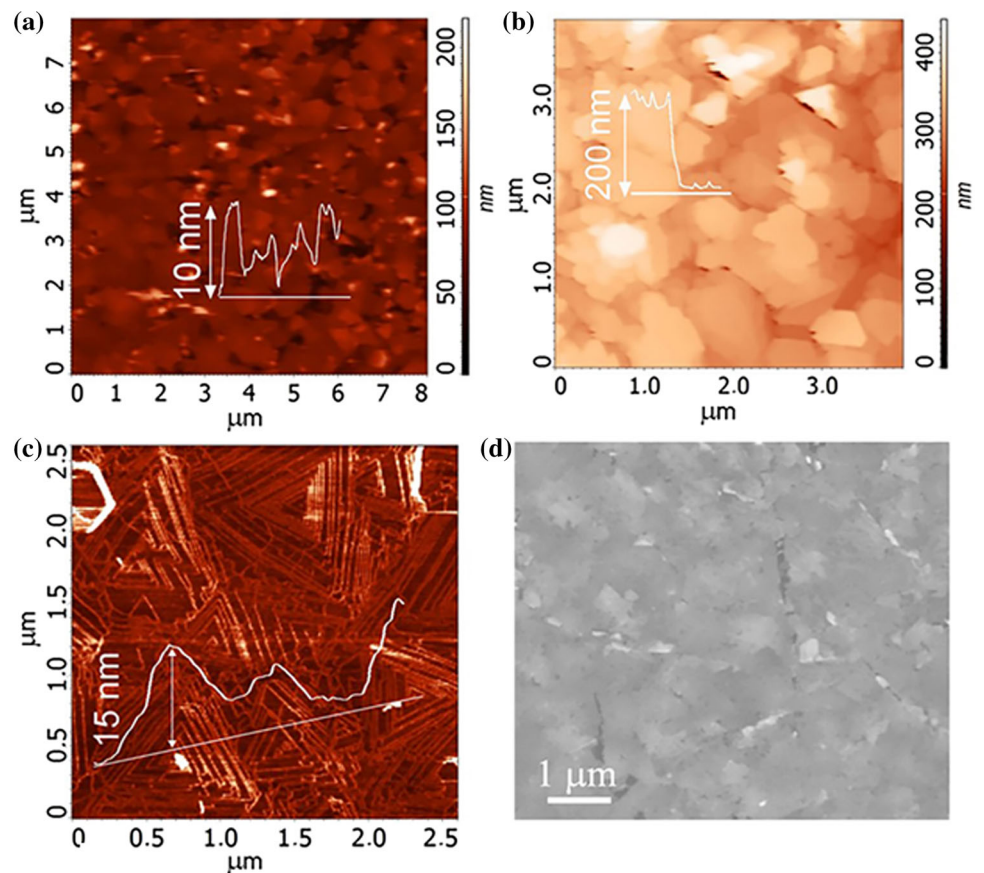

Fig. 4c have two types of orientations (right and left parts of the image).

The typical Raman spectrum of the thin Bi_2Se_3 films is given in Fig. 5a. Three characteristic peaks were observed at 71 cm^{-1}, 130 cm^{-1}, and 173 cm^{-1}, which correspond to the out-of-plane vibrational mode (A_{1g}^1) of the outer $BiSe_1$ pairs, in-plane mode (E_{g2}^2), and an out-of-plane mode (A_{1g}^2) of rhombohedra Bi_2Se_3 lattice vibrations, respectively [32]. According to Zhang, the position of Raman peak A_{1g}^1 has to be strongly dependent on the film thickness.

The position of the A_{1g}^1 peak is at 70–71 cm^{-1} for all samples up to Bi_2Se_3 thickness of 200 nm corresponding to the thickness of $\sim$ 8 QL (the thickness of the continuous film in our case). It is suggested that the Raman signal from surface states is dominated in the spectra over the contribution of the volume due to resonance scattering in the surface channel. Another finding of Zhang [32] for Bi_2Se_3 platelets is the significant thickness dependence of E_{g2}^2 line broadening (decrease in layer thickness has to lead to an increase in FWHM from $\sim$ 7.7 cm^{-1} for the bulk film to

Table 1 BS/G structures include Bi_2Se_3 layers grown on G/SiO_2 structures

Structures	Thickness d, nm	Type of conductivity	Electron mobility, cm^2/Vs	Hole mobility, cm^2/Vs	R, Ohm/sq
BS/G-1	200	n/p	1490–3480		240 (1060)
BS/G-2	50	n/p	1200–3200	860–1040	310 (860)
BS/G-3	50	n/p	330–740		480 (620)
BS/G-4	20	n/p	400–860	910	850
BS/G-5	15	n/p	760–1100	2100	400–580
BS/G-6	7–8	n/p	810–1010		500–600
BS/G-7	2–3	n/p	50–330		900–1200
vdW-BS/G-1	8	p		150	2100
vdW-BS/G-2	4	p		110	4400
BS/mica	50–200	n	30–200	–	1500–200

vdW-BS/G are the structures with electrochemically exfoliated films transferred on G/SiO_2 structures

Figure 5 The typical **a** Raman spectra and **b** X-ray diffraction spectra for Bi_2Se_3 film (BS/G-1e structure) with a thickness of 200 nm. Insert in **b** presents the Raman spectra of graphene on SiO_2/Si substrate before growth.
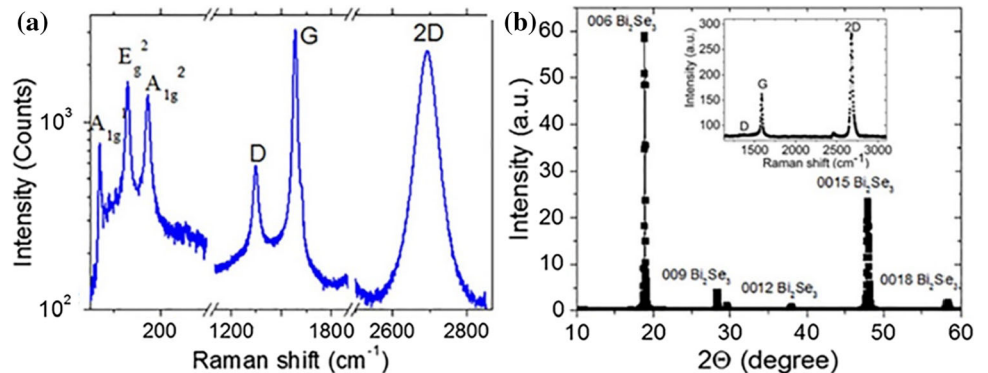
24 cm^{-1} for a 4 QL). In our case, FWHM of E_{g2}^2 mode is 7.7 cm^{-1}, i.e., it corresponds to the bulk material. We have suggested that Raman signal A_{1g}^1 from surface states is dominated in the spectra over the contribution of the volume due to resonance scattering in the surface channel, whereas E_{g2}^2 mode is based on the contribution of the film volume. The other peaks D, G, and 2D correspond to graphene [33, 34]. An increase in the D peak intensity and decrease in 2D/G ratio after Bi_2Se_3 film growth means strong changes in graphene properties (structure).

X-ray diffraction spectrum for relatively thick BS/G heterostructure is given in Fig. 5b. Samples grown at the source temperature of 500 °C show the presence of (00X) reflexes of the Bi_2Se_3 phase. This fact confirms the implementation of epitaxy Bi_2Se_3 and graphene, i.e., co-orientation of Z planes between graphene and Bi_2Se_3. Narrow lines in the spectra mean a lack of small (< 1 μm size) Bi_2Se_3 flakes or domains and a good quality of grown films.

Raman spectra measured in five random points of the BS/G-2 films at two different polarizations of the laser beam XY and YY are given in Fig. 6. One can see that relation of the E_{g2}^2 and A_{1g}^2 peak intensities given in Fig. 6 as a parameter are practically the same in all points. The variation of E_{g2}^2/A_{1g}^2 relation is equal to 3–12% for both polarizations. For comparison, Raman spectra for Bi_2Se_3 monocrystal were measured at the same point at two polarizations with crystal rotation up to 90° (step 15°). The E_{g2}^2/A_{1g}^2 relation, in this case, is varied within 21% (see Fig. 6a insert). The same values of the E_{g2}^2/A_{1g}^2 relation for different points of the grown polycrystalline film mean that domains in the film have a similar orientation. In the case of Bi_2Se_3 crystals with random orientation grown on SiO_2, the E_{g2}^2/A_{1g}^2 relation was found to equal ~ 1.

Electrical properties of heterostructures

The resistivity of the grown Bi_2Se_3 film with thickness 20–50 nm on graphene was measured lengthwise on
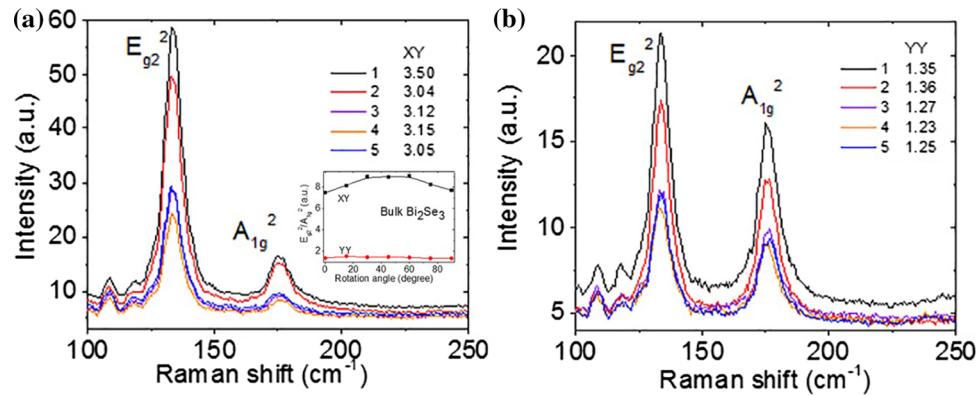
Figure 6 Raman spectra for 5 points of Bi_2Se_3 film with a thickness of 50 nm (BS/G-2 film) measured at two different polarizations **a** XY and **b** YY. The relation of E_{g2}^2 and A_{1g}^2 peak intensities is given in figures as a parameter (3.50, … in **a** and 1.35, …in **b**). The tested beam area was 30 μm. Inset in **a** demonstrates the relation of E_{g2}^2 and A_{1g}^2 peak intensities for spectra measured for one point of Bi_2Se_3 monocrystalline with its rotation.

the sample using the four-probe head. The results for one of the grown samples with a thickness of Bi_2Se_3 layer of 50–20 nm (from left to right) are shown in Fig. 7a. According to the thermal probe measurements, the Bi_2Se_3 films have n-type conductivity. The summary data for samples with different Bi_2Se_3 film thickness is given in Fig. 7b. A relatively weak decrease in resistivity is observed. This observation suggests that the conductance of the surface channel is dominated in transport for this thickness range. In Fig. 7c, a conductivity of the grown Bi_2Se_3 layer as a function of the film thickness is demonstrated. Data for the Bi_2Se_3 film grown on graphene is compared with that for thin films created using exfoliation from bulk Bi_2Se_3 monocrystalline [35]. One can see that in the grown structures, conductivity was essentially higher than that for exfoliated films. Poor mechanical properties of Bi_2Se_3 lead to the formation of structural defects in films during the exfoliation process and the decrease in conductivity. Moreover, the functional dependence of the conductivity of the Bi_2Se_3 film grown on graphene versus the film thickness is changed in comparison to well-known curve 2 for films exfoliated from bulk crystalline.

The typical $I_{ds}(V_g)$ characteristics are given for both types of contacts. Carrier mobility was calculated from the linear part of $I_{ds}(V_g)$ characteristics with the use of the expression

$$\mu = \frac{\Delta I_{DS}}{\Delta V_G} \frac{1}{C_{SiO_2} V_{DS} \frac{W}{L}} \qquad (1)$$

where C_{SiO_2} is the specific capacitance of the oxide layer on the surface of the silicon substrate (oxide thickness 300 nm, $\varepsilon \sim 3.9$), W and L are the width and length of the tested structure. Carrier mobility values calculated for different structures are given in Table 1.

In the case of thin films (< 8 nm), it was found a possibility to observe two channels with p-type and n-type conductivity simultaneously in $I_{ds}(V_g)$ characteristics (see Fig. 7d2). The values of the carrier mobility extracted from $I_{ds}(V_g)$ characteristics for both channels in the case of the first measurement are in the range of 4900–10,100 cm^2/Vs. Carrier density in the channels estimated from the Dirac point position is 1.3×10^{11} cm^{-2} for the n-type channel and 2.2×10^{11} cm^{-2} for the p-type channel. Low carrier density in Bi_2Se_3 film with thickness < 8 nm determined by the structural defects caused by the presence of a folds network in CVD grown graphene. At repeated measurements, Dirac points of both channels are shifted to higher voltages (Fig. 7d1). An increase in the carrier density in the graphene-related p-type channel was observed from $\sim 1.3 \times 10^{11}$ to $\sim 1.5 \times 10^{12}$ cm^{-2}. For the n-type channel, the carrier density is increased to a value higher than 5×10^{12} cm^{-2}. These changes are persisted at least during a few days of repeated measurements. The final $I_{ds}(V_g)$ characteristics look like curves in Fig. 7e: The only n-type channel is seen with reduced carrier mobility of 4200–400 cm^2/Vs. The physical reason for changes in carrier densities in p- and n-type channels is the formation of a double-charged layer on the BS/graphene interface due to current flow under an applied voltage.

Figure 7 a The resistivity of Bi_2Se_3 film grown on the G/SiO$_2$/Si substrate measured with the use of four probes. The position of the G/SiO$_2$ interface is marked with a vertical dotted line. The horizontal dotted line presents the resistivity of pristine graphene (1.36 kOhm/sq). Insert shows the film thickness. **b** The resistivity of Bi_2Se_3 film grown on graphene as a function of film thickness. **c** Comparison of the conductivity of grown Bi_2Se_3 film (1) and film exfoliated from Bi_2Se_3 monocrystalline (2). (d1,d2) Variation of $I_{ds}(V_g)$ characteristic for transistor structures with bottom gate (silicon) for Bi_2Se_3 film thickness of 6 nm and Ag contacts under repeated measurements. 1,2,3 is the measurement sequence with final $I_{ds}(V_g)$ characteristics like the one given in **e**. **e, f** Typical $I_{ds}(V_g)$ characteristics for transistor structures with bottom gate (silicon) for two types of contacts for structure with Bi_2Se_3 film thickness of 20 nm.
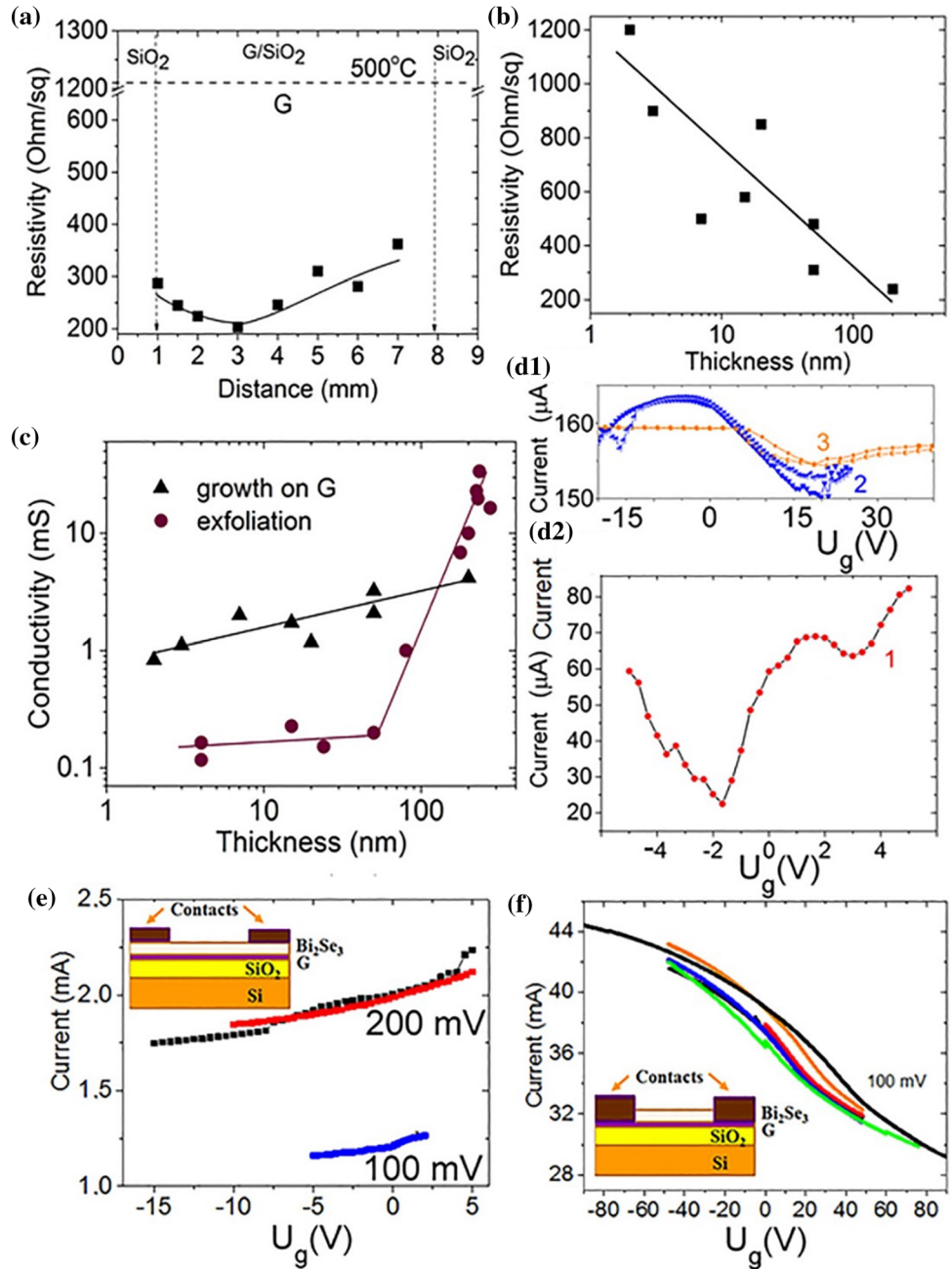
The field-effect carrier mobilities were compared with Hall effect mobility for two samples from group BS/G-3 (see Table 1). The Hall effect mobilities were equal to 270–450 cm^2/Vs (compare with 330–740 cm^2/Vs).

Two types of contacts were used to the study of the electrical properties of the heterostructures. In the first case, Ag contacts are created on the Bi_2Se_3 film surface with *n*-type conductivity. These contacts allow us to examine the properties of the Bi_2Se_3 film. Namely, this type of contact is used for the data

discussed above. In the second case, indium contacts were created and burned. As a result, we have contacts with the bottom layers of BS/G heterostructures. The existence of a *p*-type channel was observed in these BS/G heterostructures (see Fig. 7f). As mentioned above, the pristine graphene has the p-type conductivity with resistivity ∼ 0.9–1.3 kOhm/sq and carrier mobility of 1000–2000 cm^2/Vs. It is well known that graphene usually has *p*-type doping which is associated with the adsorption of oxygen on the graphene surface [36, 37]. The values

of *p*-type channel resistivity and carrier mobility extracted from our measurements and given in Table 1 are well correlated with that of pristine graphene.

Transistor characteristics for different samples with film thickness 20–200 nm measured with the use of silicon substrate as a gate look like the ones shown in Fig. 7e, f. Typical values of the electron mobility of *n*-type channels determined with the Bi_2Se_3 layer are ranged from 1500 to 3400 cm^2/Vs (see Table 1). *N*-type of Bi_2Se_3 layer is well known and attributed to native defects such as Se_{Bi} antisites and/or Se vacancies, acting as active *n*-type dopants (for instance, [38]). In the case when vdW-BS/G was created employing transfer of the exfoliated films on $G/SiO_2/Si$ substrate, the hole mobility in the Bi_2Se_3 layer is increased up to 110–150 cm^2/Vs in comparison with $BS/SiO_2/Si$ (30–50 cm^2/Vs) [35] (see Table 1). In the grown BS/G heterostructures, the carrier mobility in Bi_2Se_3 film is found to strongly increase in comparison with vdW-BS/G.

The additional treatment of the grown heterostructures in the growth camera at 500 °C and low pressure without precursor leads to the evaporation of the Bi_2Se_3 films. Unexpectedly, it was revealed that exposed graphene consists of separated islands without a network of folds observed for pristine material. It is well known that annealing of CVD graphene at 500 °C and low pressure does not lead to any visible changes in the network of folds. It means that strained graphene in folds is most likely chemically interacted with the grown Bi_2Se_3 layer, and these parts are removed simultaneously with the Bi_2Se_3 film.

The temperature dependence of resistance for two samples with different film thicknesses is shown in Fig. 8. At high temperatures, the decrease of *R* corresponds to the mobility increase with decreasing temperature (electron–phonon interaction). Then the thick (50 nm) films show a weakly metallic behavior, slightly decreasing *R* with a decrease in the temperature. Thinner films change the behavior; here resistance increases with decreasing temperature between 35 and 10 K and *R*(*T*) practically doesn't depend on the temperature at low temperatures, *T* < 8 K. Similar dependencies of conductivity were demonstrated by Chae [39]. The typical trends of the conductance of the 20 QL Bi_2Se_3 film and 3–5 QL $Bi_2Se_3/G/SiC$ heterostructures are presented in [39]. There are three temperature regions, depending on the dominant
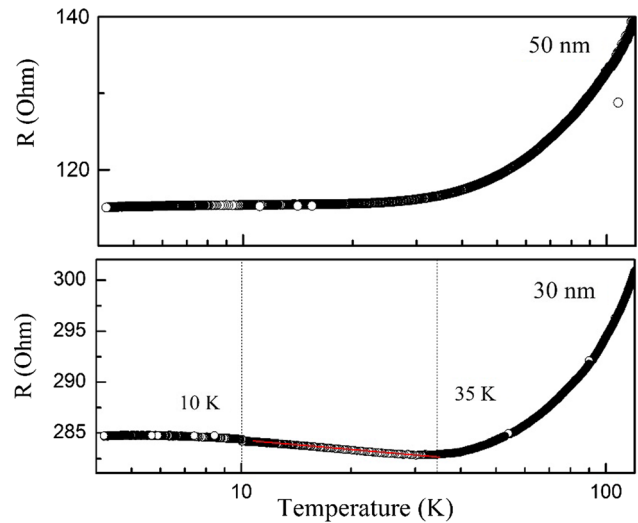

Figure 8 Temperature dependence of conductance for two samples BS/G with different film thickness 50 nm (**a**) and 30 nm (**b**).

scattering (or transport) mechanisms: electron–phonon interaction (> 20–40 K), two-dimensional electron–electron interaction (4–8 K < *T* < 20–40 K), and defect sites of the Se vacancy (< 4–8 K).

The current–voltage characteristic for structure BS/G-1 with Bi_2Se_3 film thickness of 200 nm measured for two directions of voltage sweep is given in Fig. 9. Resistivity is changed from 242 to 1070 Ω/sq. Another example of the resistivity switching for structure with Bi_2Se_3 layer thickness of 50 nm corresponds to values 310 Ω/sq and 860 Ω/sq (see Table 1, the second resistivity value is given in brackets). Structures with high carrier mobility (BS/G-1, BS/G-2, BS/G-3) demonstrate resistivity switching. This
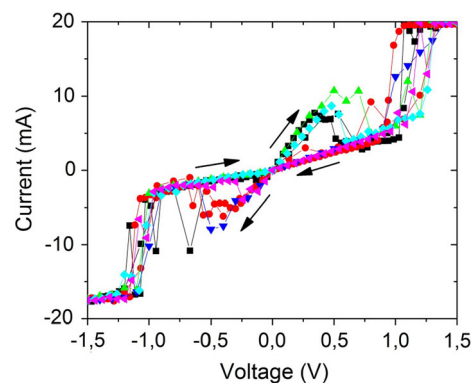

Figure 9 Current–voltage characteristics (3 repeated measurements with two-sided voltage sweeps) for structure BS/G-1 with Bi_2Se_3 film thickness of 200 nm. Resistivity is changed from 242 to 1070 Ω/sq.

switching is observed at repeated measurements and leads to *I-V* characteristics with the negative differential resistance (NDR). The appearance of NDR is suggested to base on the coexistence of *p*- and *n*-channels in our heterostructures. Similar NDR effects are observed for graphene field-effect transistors when *n–p–n* or *p–n–p* configurations along the channel are formed due to different reasons [40, 41].

Discussion

Graphene is a good substrate because of its advantages concerning film growth such as low lattice mismatch with TIs. Selective growth of Bi_2Se_3 on graphene allows one to form TI/G heterostructures on various substrates including amorphous materials by means of graphene transferring.

Another important feature of TI/G heterostructures is the good transport conductance of channels due to the charge transfer between Bi_2Se_3 and graphene even within 1 QL of Bi_2Se_3 [39]. Field-effect carrier mobility extracted from $I_{ds}(V_g)$ characteristics corresponds to channel located near Bi_2Se_3/G interface because with changing Vg charge is accumulated near the interface on a depth given by the screening length ($\lambda \sim$ 3–4 nm) [42]. According to [42], the few electron and hole channels can be found near the BS/graphene interface in the Bi_2Se_3/G heterostructures.

TI/graphene heterostructure produces a vertical *p–n* junction. We have observed the *p*-type and *n*-type channels near the BS/graphene interface in our heterostructures. Pristine graphene has *p*-type conductivity, and carrier mobility was 1000–2000 cm²/Vs. Carrier mobility in the p-type channel in our Bi_2Se_3/graphene heterostructures demonstrates similar values.

Typical values of carrier mobility for Bi_2Se_3 films with thickness 90–200 nm at room temperature are 400–700 cm²/Vs and 50–200 cm²/Vs for thickness lower than 22 nm [43–46]. At low temperature ($\sim$ 2 K), carrier mobility increases to 1200–2100 cm²/Vs [43–46]. In BS/graphene heterostructures with thick (400 nm) Bi_2Se_3 films, the carrier mobility on topological surface states was observed as high as $\sim$5000–6000 cm²/Vs at the low temperature ($\sim$ 2 K) [21, 47]. An increase in temperature leads to a strong decrease in the carrier mobility down to 50–200 cm²/Vs. High electron mobility (1500–3400 cm²/Vs)

observed at room temperature in our Bi_2Se_3/-graphene heterostructures for the n-type channel with Bi_2Se_3 thicknesses of 50–200 nm is one of the most promising properties of grown heterostructures due to proximity effects. This implies that the quality of graphene and Bi_2Se_3 could be improved in the stack structure of Bi_2Se_3/graphene. In our case, the high carrier mobility was found starting with 50 nm of Bi_2Se_3 film thickness. Even for thinner Bi_2Se_3 films in heterostructures, the carrier mobility is high enough (400–600 cm²/Vs). Carrier mobility is a very sensitive parameter determined by the quality of grown films. The achievability of the high carrier mobility is based on the quality of graphene and the used growth regime.

In various studies in the grown TI/graphene heterostructures, as a rule, individual flakes with a thickness of several QLs are analyzed [48–50]. As the present study shows, due to the island growth mechanism, a continuous film with centimeter scales is only formed starting from a thickness of 8 nm (8 QL). Thinner samples with thickness 2–6 QL and millimeter-scale size were grown and investigated. For 6 QL TI/graphene heterostructures, an increase in the carrier density in both channels is seen.

The resistivity of the n-type channel is very weak, decreased from $\sim$ 1000 to 200 Ω/sq, with an increase in Bi_2Se_3 layer thickness from 2 to 200 nm. Generally, the film conductivity $\sigma_{\square}$ is expected to decrease with reduction in film thickness *t* as $\sigma_{\square} = \sigma_{bulk} + \sigma_S$, where bulk conductivity $\sigma_{bulk} \sim t$ and σ_S is the surface channel conductivity. The sheet conductivity ($\sigma_{\square}$) for Bi_2Se_3 films versus their thickness for films created by exfoliation from bulk Bi_2Se_3 monocrystalline had demonstrated the saturation of this curve with a decrease in *t* corresponding to the value of surface channel conductivity $\sigma_{\square}$ = 0.16 mS (resistance $R_S \sim$ 8 kOhm/sq) [51]. This saturation was observed for *t* < 80 nm and corresponds to the predominant contribution of the surface channel. The thickness dependence of σ_{bulk} = 0.13*t* mS. One can see in Fig. 7c that in the case of grown TI/graphene heterostructures, functional dependence of $\sigma_{\square}$ (or $R_{\square}$) on the thickness is changed. The resistivity is slightly decreased $R_S \sim$ from 1.2 to 0.4 kOhm/sq with the increase in film thickness from 6 to 200 nm. The conductivity is described by the equation $\sigma_{\square}$ = 0.017*t* mS. We suggest that an increase in film conductivity is connected with the improvement of the quality of the Bi_2Se_3 films near the bottom

interface with graphene with the increase of grown time. This statement is suggested by the increase in carrier mobility measured for the bottom n-type channel and an increase in the Bi_2Se_3 film conductivity. This finding is a manifestation of the proximity effect in TI/graphene heterostructures. Different proximity effects are observed in vdW TI/G heterostructures. In the theoretical study of Song [16], it was demonstrated that enhancing the spin–orbit interaction in graphene, via proximity effects with topological insulators, could create a novel 2D system that combines nontrivial spin textures with high electron mobility. The spin textures of surface states in a topological insulator can be directly transferred to graphene due to the proximity effect, which is very important for realizing a two-dimensional topological insulator based on graphene [17].

It is necessary to stress the fact that the conductive channel is most likely not formed on the top surface of the grown Bi_2Se_3 films. This statement is based on the SEM and AFM images of the grown surfaces with high relief. The improvement of the bottom Bi_2Se_3/-graphene interface with the grown time increasing is seen in our experiments, and it manifests itself in the increase in conductivity and carrier mobility in the grown layer.

We have suggested that strained graphene in the network of folds interacts with a grown Bi_2Se_3 layer. It is the reason why folds are the priority place for Bi_2Se_3 growth. The high conductivity and high carrier mobility in the Bi_2Se_3 layer can be determined by the formation of the conductive channel consists of the network of some material created at the places of Bi_2Se_3 grown on folds. Interpretation of this finding requires additional research, but we have suggested that the interaction of the Bi_2Se_3 with strained graphene provides enhanced conductivity and carrier mobility.

Favorable conditions for the growth of Bi_2Se_3 films on graphene provide the possibility to fabricate Bi_2Se_3/graphene heterostructures on arbitrary substrates, where graphene can be transferred and with the required design of structures realized using graphene structuring. In combination with proximity effects, this circumstance makes the growth of Bi_2Se_3 films on graphene extremely promising for different applications. So, TI/graphene heterostructures may be a feasible way to engineer topological surface states in the heterointerface and suggest practical platforms for new functional devices. Moreover, thin

TI/G films demonstrate great potential for use in vertical 2D material heterostructures as a channel with high conductivity, instead of just graphene. The sheet resistance of TI/G films is lower than that for graphene by factor 2–10 dependently on Bi_2Se_3 thickness. One more direction of a possible application of Bi_2Se_3/graphene heterostructures is connected with utilization of structures with the negative differential resistance. The structures with the higher conductivity, carrier mobility, and the nonlinearity of the current–voltage characteristic have significant potential for the development of new functional devices for a variety of signal processing and logic applications, or IR range transparent electrodes.

Conclusions

Bi_2Se_3-based heterostructures in TI/G/SiO_2/Si configuration were created using the epitaxial growth of Bi_2Se_3 films (a physical vapor deposition method) on the CVD grown graphene. The high selectivity of a grown process on graphene in comparison with SiO_2 substrate allows one to manage the configuration of grown structures. The islands with thickness down to 1 nm are possible to grow. Films with a thickness of 2–7 nm and few millimeter scales were grown. The minimal thickness of 1 cm Bi_2Se_3 film was found to be 8 nm for the used grown regime (the source temperature of 500 °C). The existence of a graphene-related p-type conductive channel and Bi_2Se_3-related n-type conductive channel near the Bi_2Se_3/graphene interfaces were experimentally observed in all heterostructures. For all heterostructures with the Bi_2Se_3 film thickness from 2 to 200 nm, the resistivity of Bi_2Se_3 films was as low as 1000–200 Ω/sq. The high room temperature carrier mobility from 700 cm^2/Vs up to $\sim$ 3400 cm^2/Vs was observed for n-channel in films with a thickness of Bi_2Se_3 layers 7QLs and higher. The grown Bi_2Se_3/G structures were compared with the van der Waals TI/G heterostructures created by electrochemical exfoliation of Bi_2Se_3 thin layers from bulk monocrystalline with subsequent transfers onto G/SiO_2/Si substrate. The grown heterostructures demonstrate more than one order of magnitude higher carrier mobility in comparison with vdW Bi_2Se_3/G heterostructures. Moreover, the improvement of the bottom Bi_2Se_3/graphene interface with the increase in the grown time is clearly

manifested in the higher conductivity and carrier mobility in the grown layer.

The nonlinear current–voltage characteristic, high conductivity and carrier mobility of grown heterostructures provide the properties perspective not only to spintronic applications, but also for new functional devices, for a variety of signal processing and logic applications.

Acknowledgements

Compliance with ethical standards

Conflict of interest The authors declare that they have no conflict of interest.

References

[1] Geim A, Grigorieva I (2013) Van der Waals heterostructures. Nature 499:419–425. https://doi.org/10.1038/nature12385

[2] Novoselov KS, Mishchenko A, Carvalho A, Castro Neto AH (2016) 2D materials and van der Waals heterostructures. Science 353:aac9439. https://doi.org/10.1126/science.aac9439

[3] Zhu W, Park S, Yogeesh MN, Akinwande D (2017) Advancements in 2D flexible nanoelectronics: from material perspectives to RF applications. Flex Print Electron 2:043001. https://doi.org/10.1088/2058-8585/aa84a4

[4] Matsuhisa N, Chen X, Baoc Z, Someya T (2019) Materials and structural designs of stretchable conductors. Chem Soc Rev 48:2946. https://doi.org/10.1039/c8cs00814k

[5] Li X, Tao L, Chen Z, Fang H, Li X, Wang X, Xu J-B, Zhu H (2017) Graphene and related two-dimensional materials: structure-property relationships for electronics and opto-electronics. Appl Phys Rev 4:021306. https://doi.org/10.1063/1.4983646

[6] Thanh TD, Chuong ND, Hien HV, Kshetri T, Tuan LH, Kim NH, Lee JH (2018) Recent advances in two-dimensional transition metal dichalcogenides-graphene heterostructured materials for electrochemical applications. Prog Mat Sci 96:51–85. https://doi.org/10.1016/j.pmatsci.2018.03.007

[7] Miwa JA, Dendzik M, Grønborg SS, Bianchi M, Lauritsen JV, Hofmann P, Ulstrup S (2015) Van der Waals epitaxy of two-dimensional MoS_2/graphene heterostructures in a ultra-high vacuum. ACS Nano 9:6502–6510. https://doi.org/10.1021/acsnano.5b02345

[8] Woods JM, Jung Y, Xie YJ, Liu W, Liu Y, Wang H, Cha JJ (2016) One-step synthesis of MoS_2/WS_2 layered heterostructures and catalytic activity of defective transition metal dichalcogenide films. ACS Nano 10:2004–2009. https://doi.org/10.1021/acsnano.5b06126

[9] Zhang C, Li C, Yu J, Jiang S, Xu S, Yang C, Liu YJ, Gao X, Liu A, Man B (2018) SERS activated platform with three-dimensional hot spots and tunable nanometer gap. Sens Actuat B Chem 258:163–171. https://doi.org/10.1016/j.snb.2017.11.080

[10] Lewin M, Hauer B, Bornhöfft M, Jung L, Benke J, Michel A-KU, Mayer J, Wuttig M, Taubner T (2015) Imaging of phase change materials below a capping layer using correlative infrared near-field microscopy and electron microscopy. Appl Phys Lett 107:151902. https://doi.org/10.1063/1.4933102

[11] Tian W, Yu W, Shi J, Wang Y (2017) The property, preparation and application of topological insulators: a review. Materials 10:814. https://doi.org/10.3390/ma10070814

[12] Khokhriakov D, Cummings AW, Song K et al (2018) Tailoring emergent spin phenomena in Dirac material heterostructures. Sci Adv 4:eaat9349. https://doi.org/10.1126/sciadv.aat9349

[13] Qu D, Hor Y, Xiong J et al (2010) Quantum oscillations and hall anomaly of surface states in the topological insulator Bi_2Te_3. Science 329:821–824. https://doi.org/10.1126/science.1189792

[14] Chiatti O, Riha C, Lawrenz D et al (2016) 2D layered transport properties from topological insulator Bi_2Se_3 single crystals and micro flakes. Sci Rep 6:27483. https://doi.org/10.1038/srep27483

[15] He L, Xiu F, Yu X et al (2012) Surface-dominated conduction in a 6 nm thick Bi_2Se_3 thin film. Nano Lett 12:1486–1490. https://doi.org/10.1021/nl204234j

[16] Song K, Soriano D, Cummings AW et al (2018) Spin proximity effects in graphene/topological insulator heterostructures. Nano Lett 18:2033–2039. https://doi.org/10.1021/acs.nanolett.7b05482

[17] Zhang L, Yan Y, Wu H-C et al (2016) Gate-tunable tunneling resistance in graphene/topological insulator vertical junctions. ACS Nano 10:3816–3822. https://doi.org/10.1021/acsnano.6b00659

[18] Cao W, Zhang R-X, Tang P, et al (2016) Heavy Dirac fermions in a graphene/topological insulator hetero-junction.

2D Mater 3:034006. https://doi.org/10.1088/2053-1583/3/3/034006

[19] Qiao H, Yuan J, Xu Z et al (2015) Broadband photodetectors based on graphene-Bi$_2$Te$_3$ heterostructure. ACS Nano 9:1886–1894. https://doi.org/10.1021/nn506920z

[20] Vaklinova K, Hoyer A, Burghard M, Kern K (2016) Current-induced spin polarization in topological insulator-graphene heterostructures. Nano Lett 16:2595–2602. https://doi.org/10.1021/acs.nanolett.6b00167

[21] Kim N, Lee P, Kim Y et al (2014) Persistent topological surface state at the interface of Bi$_2$Se$_3$ film grown on patterned graphene. ACS Nano 8:1154–1160. https://doi.org/10.1021/nn405503k

[22] Lin Y, Dimitrakopoulos C, Farmer D et al (2010) Multicarrier transport in epitaxial multilayer graphene. Appl Phys Lett 97:112107. https://doi.org/10.1063/1.3485671

[23] Steinberg H, Gardner D, Lee Y, Jarillo-Herrero P (2010) Surface state transport and ambipolar electric field effect in Bi$_2$Se$_3$ nanodevices. Nano Lett 10:5032–5036. https://doi.org/10.1021/nl1032183

[24] Ren Z, Taskin A, Sasaki S et al (2010) Large bulk resistivity and surface quantum oscillations in the topological insulator Bi$_2$Te$_2$Se. Phys Rev B 82:241306. https://doi.org/10.1103/PhysRevB.82.241306

[25] Lee P, Jin KH, Sung SJ et al (2015) Proximity effect induced electronic properties of graphene on Bi$_2$Te$_2$Se. ACS Nano 9:10861–10866. https://doi.org/10.1021/acsnano.5b03821

[26] Liu G, Rumyantsev SL, Shur MS, Balandin AA (2013) Origin of 1/f noise in graphene multilayers: surface vs. volume. Appl Phys Lett 102:093111. https://doi.org/10.1063/1.4794843

[27] Bøggild P, Mackenzie DMA, Whelan PR, et al (2017) Mapping the electrical properties of large-area graphene. 2D Mater 4:042003. https://doi.org/10.1088/2053-1583/aa8683

[28] Cultrera A, Serazio D, Zurutuza A et al (2019) Mapping the conductivity of graphene with electrical resistance tomography. Sci Rep 9:10655. https://doi.org/10.1038/s41598-019-46713-8

[29] Peng HL, Dang WH, Cao J et al (2012) Topological insulator nanostructures for near-infrared transparent flexible electrodes. Nat Chem 4:281–286. https://doi.org/10.1038/nchem.1277

[30] Min Y, Moon GD, Kim BS et al (2012) Quick, controlled synthesis of ultrathin Bi$_2$Se$_3$ nanodiscs and nanosheets. J Am Chem Soc 134:2872–2875. https://doi.org/10.1021/ja209991z

[31] Hong SS, Kundhikanjana W, Cha JJ et al (2010) Ultrathin topological insulator Bi$_2$Se$_3$ nanoribbons exfoliated by atomic force microscopy. Nano Lett 10:3118–3122. https://doi.org/10.1021/nl101884h

[32] Zhang J, Peng ZP, Soni A et al (2011) Raman spectroscopy of few quintuple layer topological insulator Bi2Se3 nanoplatelets. Nano Lett 11:2407–2414. https://doi.org/10.1021/nl200773n

[33] Ryu S, Maultzsch J, Han MY et al (2011) Raman spectroscopy of lithographically patterned graphene nanoribbons. ACS Nano 5:4123–4130. https://doi.org/10.1021/nn200799y

[34] Ferrari AC, Robertson J (2000) Interpretation of Raman spectra of disordered and amorphous carbon Phys. Rev B 61:14095. https://doi.org/10.1103/PhysRevB.61.14095

[35] Antonova IV, Nebogatikova NA, Kokh KA et al (2020) Electrochemically exfoliated thin Bi$_2$Se$_3$ films and van der Waals heterostructures Bi$_2$Se$_3$/graphene. Nanotechnology 31:125602. https://doi.org/10.1088/1361-6528/ab5cd5

[36] Piazza A, Giannazzo F, Buscarino G, Fisichella G, La Magna A, Roccaforte F, Cannas M, Gelardi FM, Agnello S (2015) Graphene p-type doping and stability by thermal treatments in molecular oxygen controlled atmosphere. J Phys Chem C 119:22718–22723. https://doi.org/10.1021/acs.jpcc.5b07301

[37] Liu H, Liu Y, Zhu D (2011) Chemical doping of graphene. J Mater Chem 21:3335–3345. https://doi.org/10.1039/C0JM02922J

[38] Xue L, Zhou P, Zhang CX, He CY, Hao GL, Sun LZ, Zhong JX (2013) First-principles study of native point defects in Bi$_2$Se$_3$. AIP Adv 3:052105. https://doi.org/10.1063/1.4804439

[39] Chae J, Kang S-H, Park SH et al (2019) Closing the surface bandgap in thin Bi$_2$Se$_3$/graphene heterostructures. ACS Nano 13:3931–3939. https://doi.org/10.1021/acsnano.8b07012

[40] Grassi R, Low T, Gnudi A, Baccarani G (2013) Contact-induced negative differential resistance in short-channel graphene FETs IEEE Trans. Electron Devices 60:140–146. https://doi.org/10.1109/TED.2012.2228868

[41] Tran PX (2018) Modulation of negative differential resistance in graphene field-effect transistors by tuning the contact resistances. J Electron Mater 47:5905–5912. https://doi.org/10.1007/s11664-018-6480-6

[42] Sacépé B, Oostinga JB, Li J et al (2011) Gate-tuned normal and superconducting transport at the surface of a topological insulator. Nat Commun 2:575. https://doi.org/10.1038/ncomms1586

[43] Wang S, Li Y, Ng A, Hu Q, Zhou Q, Li X, Liu H (2020) 2D Bi$_2$Se$_3$ van der Waals epitaxy on mica for optoelectronics applications. Nanomaterials 10:1653. https://doi.org/10.3390/nano10091653

[44] Li HD, Wang ZY, Kan X, Guo X, He HT, Wang Z, Wang JN, Wong TL, Wang N, Xie MH (2010) The van der Waals epitaxy of Bi$_2$Se$_3$ on the vicinal Si(111) surface: an approach

for preparing high-quality thin films of a topological insulator. New J Phys 12:103038. https://doi.org/10.1088/1367-2630/12/10/103038

[45] Kamboj VS, Singha A, Ferrusb T, Beerea HE, Duffyc LB, Hesjedalc T, Barnesa CHW, Ritchie DA (2017) Probing the topological surface state in Bi2Se3 thin films using temperature-dependent terahertz spectroscopy. ACS Photonics 4:2711–2718. https://doi.org/10.1021/acsphotonics.7b00492

[46] Brahlek M, Kim YS, Bansal N, Edrey E, Oh S (2011) Surface versus bulk state in topological insulator Bi2Se3 under environmental disorder. Appl Phys Lett 99:012109. https://doi.org/10.1063/1.3607484

[47] Bianchi M, Guan D, Bao S et al (2010) Coexistence of the topological state and a two-dimensional electron gas on the surface of Bi$_2$Se$_3$. Nat Commun 1:128. https://doi.org/10.1038/ncomms1131

[48] Zhang L, Lin B-C, Wu Y-F et al (2017) Electronic coupling between graphene and topological insulator induced anomalous magnetotransport properties. ACS Nano 11:6277–6285. https://doi.org/10.1021/acsnano.7b02494

[49] Dang W, Peng H, Li H et al (2010) Epitaxial heterostructures of ultrathin topological insulator nanoplate and graphene. Nano Lett 10:2870–2876. https://doi.org/10.1021/nl100938e

[50] Zhang C, Liu M, Man BY et al (2014) Facile fabrication of graphene-topological insulator Bi$_2$Se$_3$ hybrid Dirac materials via chemical vapor deposition in Se-rich conditions. Cryst Eng Commun 16:8941–8945. https://doi.org/10.1039/C4CE01269K

[51] Suna Z, Mana B, Yanga C et al (2016) Selenium-assisted controlled growth of graphene–Bi$_2$Se$_3$ nanoplates hybrid Dirac materials by chemical vapor deposition. Appl Surf Sci 365:357–363. https://doi.org/10.1016/j.apsusc.2015.12.212